Drag Coefficient of a Non-Convex Polygonal Plate during Free Fall

Yoshihiro Kubota[1], Yuhei Endo[2]

[1]Department of Mechanical Engineering, Toyo University, Kawagoe, Japan
[2]Graduate School of Science and Engineering, Toyo University, Kawagoe, Japan
Email: kubota548@toyo.jp

Abstract

Waterside creatures or aquatic organisms use a fin or web to generate a thrust force. These fins or webs have a non-convex section, referred to as a non-convex shape. We investigate the drag force acting on a non-convex plate during unsteady motion. We perform the experiment in a water tank during free fall. We fabricate the non-convex plate by cutting isosceles triangles from the side of a convex hexagonal plate. The base angle of the triangle is between 0° to 45°. The base angle is 0 indicates the convex hexagonal thin plate. We estimate the drag coefficient with the force balance acting on the model based on the image analysis technique. The results indicate that increasing the base angle by more than 30° increased the drag coefficient. The drag coefficient during unsteady motion changed with the growth of the vortex behind the model. The vortex has small vortices in the shear layer, which is related to the Kelvin-Helmholtz instabilities.

Keywords

Drag Coefficients, Freefall, Image Analysis, Non-Convex Polygonal Plate, Unsteady Motion, Vortex Formation

1. Introduction

The waterside creatures or aquatic organisms use the fin or web to generate a propulsive force. The mechanism for producing a thrust force differs between terrestrial and aquatic mammals [1]. The terrestrial mammals use drag-based propulsion via paddling appendages, whereas aquatic mammals use lift-based propulsion via an oscillating hydrofoil. Wolfgang *et al.* studied the relationship between the generation of propulsive force and the flow around the fish [2]. They investigated the unsteady two-dimensional velocity field experimentally

and the three-dimensional velocity field numerically. They visualized the flow around the non-convex portion of a tail fin during swimming. They discussed the relationship between dorsal, pectoral, and tail fins. Borazjani and Daghooghi reported the effect of the shape of the fish tail fin on the lift-based propulsive force generation [3]. They conducted the numerical simulation with a non-convex tail fin (e.g., shark tail), convex triangular fin, and rectangular tail fin. They formed the stable leading-edge vortex with a non-convex fin and a convex triangular fin. The formation of the trailing edge vortex influenced the convexity. However, they did not discuss the details of the influence. They also mentioned the propulsion force generated with paddling in the drag-based propulsion. The duck and the frog use the paddle to move forward. Johansson and Norberg reported the foot-propelled swimming by a bird's propulsion [4]. They demonstrated that the propulsive force is obtained by drag force when the foot web becomes perpendicular at the beginning of the power stroke. After the power stroke phase, the mechanism used to generate the propulsive force gradually shifts to lift-based propulsion. The relation between force generation and the flow around the paddle or fin is related to the propulsion. However, they did not discuss the influence of shape. Kikuchi *et al.* demonstrated the relationship between the fish fin shape and thrust generation [5]. They obtained the results using a convex polygonal thin plate. However, the paddle of aquatic organisms has a web, and the shape of the paddle is non-convex. Nedic *et al.* studied the effect of fractal edge geometry on drag and wake [6]. They used the fractal thin plate which had the non-convex part to measure the drag coefficient. The drag coefficient of fractal plate is 1.18 at the fractal dimension is 1.3. Also, they discovered that as the fractal dimension and plate perimeter increased, the drag coefficient increased by up to 7%. To understand the flow around a complex shape, we must first understand the influence of factors (such as convexity and the number of edges) on the fishtail. The influence of the number of edges was studied as shown above. However, the strength of convexity has not been discussed yet.

The paddling motion is the complicated synchronous motion between body and fin dynamics [2]. This study provides the drag coefficient and visualization before understanding a more complicated model. Therefore, we considered free-falling for the measurement. Xiang *et al.* investigated the trajectory of freely falling plates by the momentum of inertia and Reynolds number [7]. They observed four modes of trajectories. The trajectories corresponded to the wake. The phase diagram of the moment of inertia and Reynolds number showed wake instability. Lau *et al.* studied the complex formation and dissipation of large-scale vortical structures during the freely falling plate [8]. Karman vortex pairs or Kelvin-Helmholtz instabilities are found in a trailing flow structure. This freely falling plate affects the unsteadiness with the formation of the wake. He and Liu studied the shear layer of a round jet [9]. They conducted the unsteady large-scale flow structure using the planar-laser-induced fluorescence technique. Fu *et al.* studied the shear layer of a jet in an axisymmetric container [10]. They demonstrated a high velocity fluctuation and vorticity in the shear layer. These results

show that the flow in the shear layer affects the unsteady flow structure. This unsteadiness causes the change of drag force acting on the object. Therefore, the unsteady phenomena need to be understood. However, the unsteady phenomena around the non-convex plate have not been studied yet.

In this study, we estimate the drag force acting on a non-convex thin flat plate during free fall. We fabricate the non-convex plate by cutting isosceles triangles from the edge of a convex hexagonal plate. We consider the influence of non-convexity with the base angle of isosceles triangles. We visualize the flow structure around the model with the fluorescent dye solution to understand the vortex formation during unsteady motion.

2. Experimental Setup

Figure 1 shows the experimental setup. A water tank ($450 \times 450 \times 600$ mm) was filled with water up to a height of 400 mm from the bottom. A guide rod was attached to the model and dropped freely from a height of 350 mm. Simultaneously, a pulley was used to prevent horizontal movement. Because the model was accelerated with the gravity from rest, it had an unsteady motion. The model motion was captured using a high-speed camera (Miro LAB 310, Vision Research, Inc.) at 100 frames per second. An LED light bulb was used as the light source from the side of the water tank to shorten the exposure time and thus reduce the roughness of the image. The image was used for the image analysis, and the motion was analyzed from the position of the model at every 0.01 s. The experiment was performed ten times in total for each model. We applied the image analysis results to estimate the drag force acting on the model based on the force balance.

We can express the force balance of the freely falling plate as (1). The notation D is the drag force, B is the buoyancy, W is the gravitational force, m is the mass of the model, V is the volume of the model, A is the projected area of the model, ρ_w is the density of water, u is the velocity of the model, g is the gravitational acceleration, and C_d is the drag coefficient.
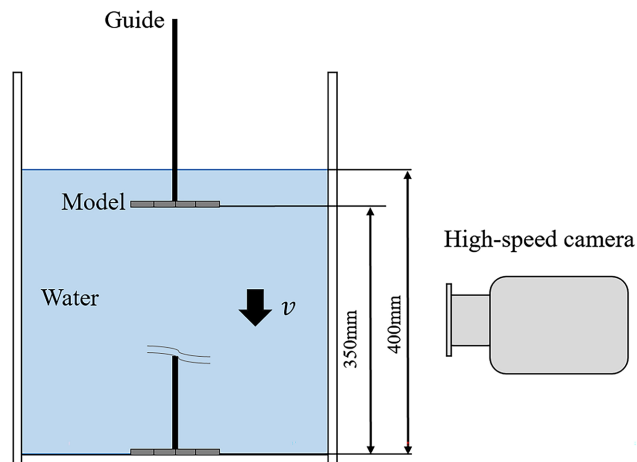

Figure 1. Sketch of the experimental setup.

$$ma = W - D - B \tag{1}$$

Equation (1) can be rewritten as (2).

$$m\frac{\mathrm{d}u}{\mathrm{d}t} = mg - C_d\frac{1}{2}\rho_{\mathrm{w}}u^2 A - \rho_{\mathrm{w}}gV \tag{2}$$

Further, we can obtain the drag coefficient from (2) as follows:

$$C_d = \frac{2}{\rho u^2 A}\left(mg - m\frac{\mathrm{d}u}{\mathrm{d}t} - \rho_{\mathrm{w}}gV\right). \tag{3}$$

This means that if we know the time series of the velocity of an object, we can estimate the drag coefficient. In this study, we derived the change at the time of the free-fall speed of an object and derived the drag coefficient through image analysis. We obtained the acceleration from the difference in speed using the fourth-order center difference method and derived the drag coefficient C_d. **Figure 2** shows the flowchart of experimental procedures to understand the experimental process easily. The notation in flowchard L is the traveling distance of model, i is the number of trials and j is the frame number of images in each trial. **Table 1** shows the performance metrics for the evaluation of measurement [11]. The notation n is the number of data.

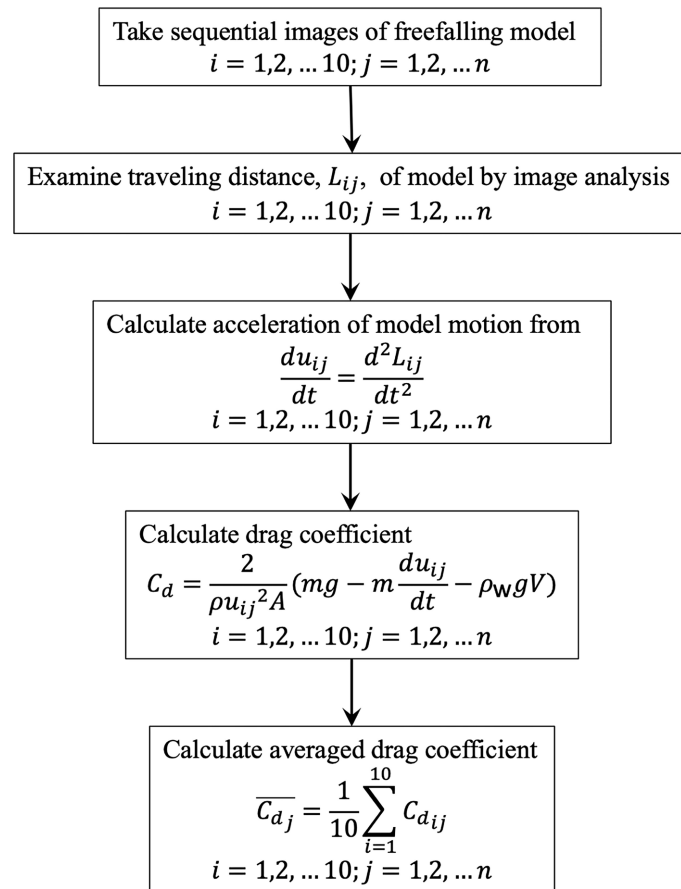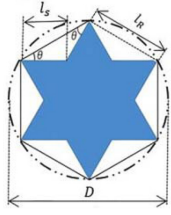We performed the experiment using ten types of models. **Table 2** shows the

Take sequential images of freefalling model
$i = 1,2,\ldots 10; j = 1,2,\ldots n$

↓

Examine traveling distance, L_{ij}, of model by image analysis
$i = 1,2,\ldots 10; j = 1,2,\ldots n$

↓

Calculate acceleration of model motion from
$$\frac{du_{ij}}{dt} = \frac{d^2 L_{ij}}{dt^2}$$
$i = 1,2,\ldots 10; j = 1,2,\ldots n$

↓

Calculate drag coefficient
$$C_d = \frac{2}{\rho u_{ij}{}^2 A}(mg - m\frac{du_{ij}}{dt} - \rho_{\mathrm{w}}gV)$$
$i = 1,2,\ldots 10; j = 1,2,\ldots n$

↓

Calculate averaged drag coefficient
$$\overline{C_{dj}} = \frac{1}{10}\sum_{i=1}^{10} C_{d_{ij}}$$
$i = 1,2,\ldots 10; j = 1,2,\ldots n$

Figure 2. Procedures of measurement.

Table 1. Performance metrics of measurement.

Metrics	Expression	Range	Remarks
Averaged C_d	$\overline{C_{d_j}} = \dfrac{1}{10}\sum\limits_{i=1}^{10} C_{d_{ij}}$	$-\infty \leq \overline{C_{d_j}} \leq \infty$	
Standard Deviation	$SD = \sqrt{\dfrac{\sum\left(C_{d_{ij}} - \overline{C_{d_j}}\right)^2}{n-1}}$	$-\infty \leq SD \leq \infty$	
Skewness	$SKEW = \dfrac{n}{(n-1)(n-2)}\sum\left(\dfrac{C_{d_{ij}} - \overline{C_{d_j}}}{SD}\right)^3$	$-\infty \leq SKEW \leq \infty$	
Coefficient of variation	$CV = \dfrac{SD}{\overline{C_{d_j}}}$	$-\infty \leq CV \leq \infty$	
Confidence intervals	$CI = \overline{C_{d_j}} \pm 1.96\left(\dfrac{SD}{\sqrt{n}}\right)$	$-\infty \leq CI \leq \infty$	Confidence coefficient, α, is 5%.

Table 2. Sketches of the models.

Specification of model	$\theta = 0°$	$\theta = 5°$	$\theta = 10°$	$\theta = 15°$
	model$_{0°}$	model$_{5°}$	model$_{10°}$	model$_{15°}$

$\theta = 20°$	$\theta = 25°$	$\theta = 30°$	$\theta = 35°$	$\theta = 40°$	$\theta = 45°$
model$_{20°}$	model$_{25°}$	model$_{30°}$	model$_{35°}$	model$_{40°}$	model$_{45°}$

sketch of each model. We obtained the models from a convex hexagonal thin plate. All the obtained models were flat plates. We determined the convex in the model at the edge of the plate. We fabricated the non-convex model by cutting off isosceles triangles from the edge of the convex hexagonal plate; this means that the base angle of the triangle $\theta = 0°$. Thus, we call the convex model as model$_{0°}$ shown in Table 2. We determined nine types of base angles for the non-convex model between $5° \leq \theta \leq 45°$ at every 5°. The material of the model was an acrylic plate. The density of the acryl resin was 1.18 g/cm³. All models had the same projected area (2.3×10^3 mm²) and thickness (2 mm). The model sizes differed in appearance to maintain a constant projected area. Because the models had the same volume, their mass and buoyancy were the same. Table 3 contains additional information about the model geometries. The notation of length in l_s, l_R, and D corresponds to Table 2. l_s is the length of the equal sides in an isosceles triangle. l_R is the length of the edge in a convex hexagon. D is the diameter of the

Table 3. Geometries of the models.

model	θ (degree)	Area (mm^2)	l_s (mm)	l_R (mm)	D (mm)
model$_{0°}$	0	2.3×10^3	15.0	30.0	60.0
model$_{5°}$	5	2.3×10^3	15.5	30.8	61.6
model$_{10°}$	10	2.3×10^3	16.1	31.7	63.3
model$_{15°}$	15	2.3×10^3	16.9	32.6	65.3
model$_{20°}$	20	2.3×10^3	18.0	33.8	67.5
model$_{25°}$	25	2.3×10^3	19.4	35.1	70.2
model$_{30°}$	30	2.3×10^3	21.2	36.7	73.5
model$_{35°}$	35	2.3×10^3	23.7	38.9	77.7
model$_{40°}$	40	2.3×10^3	27.3	41.8	83.6
model$_{45°}$	45	2.3×10^3	32.6	46.1	92.3

circumscribed circle in the model. We obtained the drag coefficient using these estimation models and through image analysis. We performed the flow visualization to understand the relationship between the drag coefficient and the flow structure around the model. We visualized the flow structure with the uranin solution mixed with water-soluble glue. We painted the bottom face of the model with the solution. We illuminated the three-dimensional flow structure with the UV LED to understand the overall flow structure behind the model because the geometry of the model evokes the three-dimensional vortex structure with the non-convex shape. The wavelength of the light source was 365 nm. Further, we illuminated the flow structure for the cross-section with a laser light sheet (PIV Laser, Kato Koken Co., Ltd.). The thickness of the sheet was around 1 mm, and the wavelength was 532 nm.

3. Results and Discussion

We estimated the drag coefficient by measuring the time series of the falling velocity of the model, as explained in the previous section. **Figure 3** shows the results of the time series of the falling velocity. It shows the relationship between the vertical falling velocity of the model and time. The symbols show the average value of ten trials. The error bar shows the standard deviation of the trials. The figure shows the results of model$_{0°}$, model$_{15°}$, model$_{30°}$, and model$_{45°}$. The results from these models show the discriminative for understanding the influence on the strength of convexity. Therefore, we will use these results for the discussion. Time measurement starts at the release from the steady condition of the model. All results indicated that the models were initially accelerated, and further, the change in velocity became smaller. Finally, the velocity reached terminal velocity. The difference in the slope of velocity in time ≤ 0.4 s was not observed among the model motions. The difference in magnitude of velocity was observed when the time was greater than 0.4 s. The magnitude of the terminal velocity of model$_{45°}$ was the minimum compared with the other models. The difference in magnitude
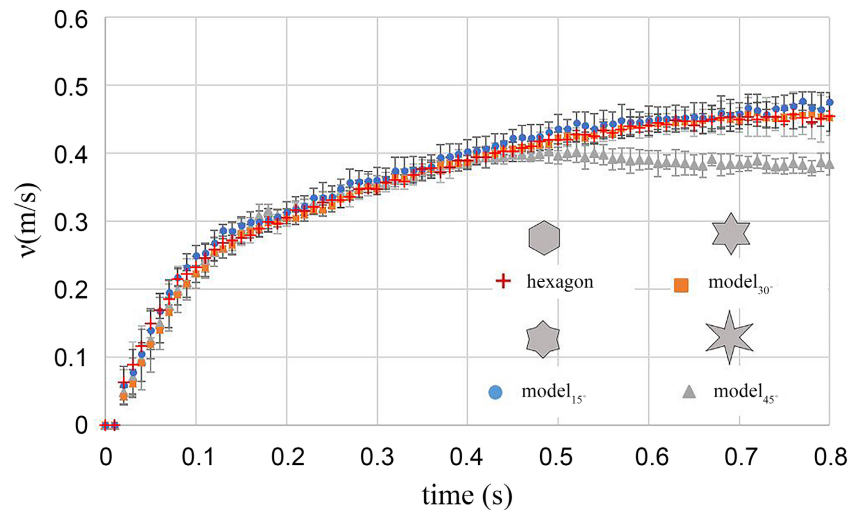
Figure 3. Time series of the falling velocity of the model. The symbols show the experimental results.

of the terminal velocity can be explained by the force balance acting on the model. **Figure 4** shows the free body diagram. The gravitational force W, the buoyancy force B, and the drag force D were acting on the model at the terminal velocity, as shown in the figure. All models had the same volume and material; this means that the gravitational force and buoyancy were not different because the mass and density of the model were the same. Thus, the difference in magnitude of the terminal velocity arises from the difference in drag force. The drag coefficient of the model will be discussed later. Furthermore, the terminal velocity was constant in the theoretical method. However, the falling velocity in our case was fluctuating after the acceleration phase (e.g., time > 0.4 s in $model_{45°}$) due to the change in drag force during the free fall. This will be discussed later.

Figure 5 shows the result of the estimated drag coefficient. The symbols in the figure correspond to the shape of the experimental models. We calculated the drag coefficient at the terminal velocity phase, as shown in **Figure 3**. The results were the average of the ten trials. The error bar shows the standard deviation of the measurements. We calculated the drag coefficient from (3) at the terminal velocity, as shown in **Figure 3**. The horizontal axis in the figure is the base angle of the isosceles triangle, which is cut off from the convex hexagon to investigate the non-convex models. The drag coefficient at $\theta \leq 30°$ was almost constant despite the change in base angle. Contrarily, the results in $\theta > 30°$ increased with the base angle. Further, the statistical properties of results are shown in **Table 4**. Thus, we determined the drag coefficient of the non-convex model during the terminal velocity. How does it perform the drag coefficient during unsteady motion?

Figure 6 shows the relationship between the drag coefficient and Reynolds number, Re. Re is defined as uL/ν, where L is the equivalent diameter of the model and ν is the kinematic viscosity. We used the averaged velocity as the characteristic velocity u in the formula for the Reynolds number. We obtained
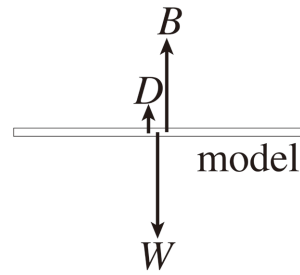
Figure 4. Free body diagram of the model under the terminal velocity.
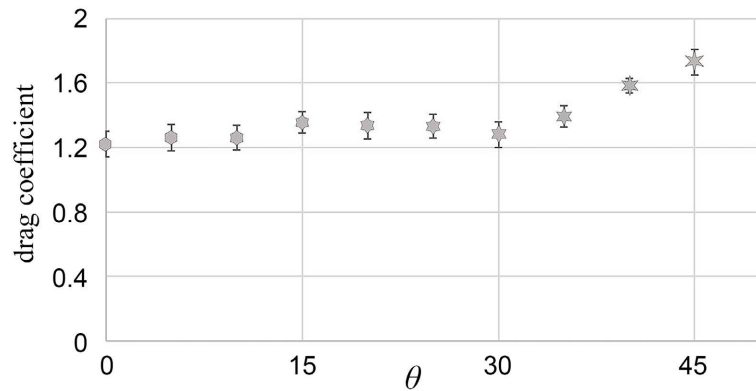

Figure 5. Relationship between the drag coefficient and the base angle of the non-convex part.
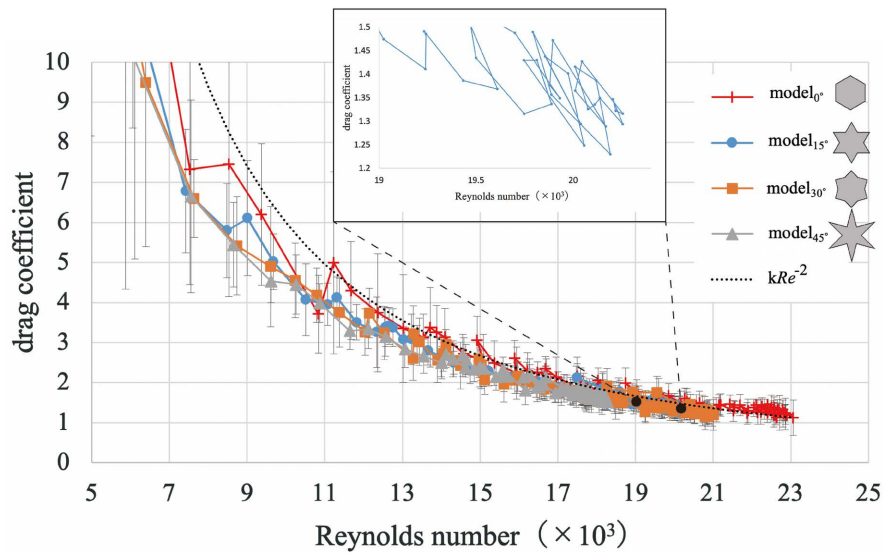
Figure 6. Change in drag coefficient with free falling.

the equivalent diameter from $L = (\text{projection area}/\pi)^{0.5}$. The projection area was the same in all the models, as shown in **Table 2**, such that the characteristic length was also the same for obtaining the Reynolds number. We calculated the drag coefficient with the averaged velocity in each timing from the model release; further, we averaged the value with ten trials. The error bar in the figure represents the standard deviation. The solid line connection shows the progress

Table 4. Statistical properties of measurements.

Model	average C_d	standard deviation of C_d	Min. C_d	Max. C_d	median value of C_d	skewness	coefficient of variation	confidence intervals
model$_{0°}$	1.25	0.277	0.442	2.02	1.22	0.420	0.224	0.172
model$_{5°}$	1.26	0.218	0.303	2.73	1.27	0.0122	0.172	0.135
model$_{10°}$	1.26	0.247	0.702	2.18	1.23	0.576	0.196	0.153
model$_{15°}$	1.36	0.192	0.835	2.25	1.35	0.162	0.137	0.116
model$_{20°}$	1.33	0.186	0.862	1.92	1.33	0.128	0.140	0.115
model$_{25°}$	1.34	0.195	0.856	2.01	1.34	0.248	0.144	0.120
model$_{30°}$	1.28	0.240	0.564	2.17	1.24	0.276	0.189	0.149
model$_{35°}$	1.40	0.205	0.771	2.07	1.39	0.211	0.147	0.127
model$_{40°}$	1.59	0.262	1.033	2.42	1.58	0.249	0.166	0.163
model$_{45°}$	1.73	0.265	1.116	2.48	1.74	0.200	0.153	0.164

in time because the Reynolds number loses the information of time. The small window in the figure shows the enlarged view of the results with model$_{15°}$ at $18 \times 10^3 < Re < 20 \times 10^3$. In the acceleration phase, the drag coefficient of all models decreased with the Reynolds number. Breidenthal investigated the effect of acceleration on turbulent entrainment, which showed that acceleration reduces the entrainment rate of turbulent vortices [12]. How does the acceleration affect the drag coefficient in this setup? If the acceleration ($= du/dt$) is constant, the drag coefficient can be rewritten as kRe^{-2} because the drag coefficient is the function of u^{-2} from (3), where k is the constant value depending on model geometry and physical property of the experimental setup. We plot kRe^{-2} by a dotted line in **Figure 5**. The constant value k was varied to fit the model$_{0°}$. The slope of kRe^{-2} and the experimental results appeared similar; however, they fluctuated around kRe^{-2}. This relationship indicates the trend of drag coefficient depending on the velocity and magnitude of the drag coefficient depending on the acceleration. Therefore, this fluctuation of the drag coefficient is related to the effect of acceleration.

Finally, the estimated drag coefficient became asymptotic to the value of terminal velocity. From the enlarged view in the figure for the result by model$_{15°}$, we can observe the change in drag coefficient with the change in Reynolds number with the periodical motion. Kikuchi *et al.* described the periodical change in drag coefficient using a free-falling spherical body [13]. They investigated the relationship between the change in drag coefficient and the flow structure around the model.

Figure 7 shows the results from the flow visualization with the uranin solution. We visualized the flow using model$_{15°}$. We observed the flow from two types of positions. One was parallel to the model and was called the 0° view, as shown in **Figure 7(a)**, **Figure 7(c)**. The other was 30° inclined to the parallel to the model and was called the 30° view, as shown in **Figure 7(b)**. The broken line
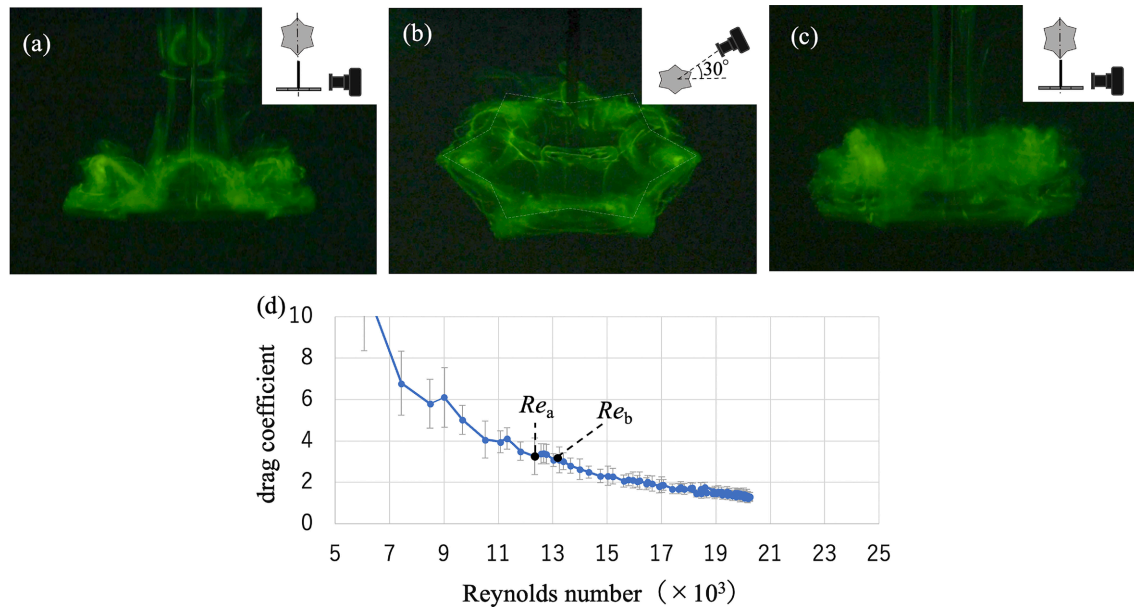
Figure 7. Dye-flow visualization using model$_{15°}$ to understand the relationship between unsteady motion and the change in the drag coefficient. (a) Side view (0˚ view) of the flow structure at $Re = Re_a$. (b) 30˚-inclined view (30˚ view) of the flow structure at $Re = Re_a$. (c) 0˚ view of the flow structure at $Re = Re_b$.

in the 30˚ view indicates the geometry of the model. The plot shown in **Figure 7(d)** corresponds to the result from **Figure 6**. These results focus on the timing around the fluctuation of the drag coefficient by the effect of acceleration during the free fall. This fluctuation appears like a small positive peak of the drag coefficient. Just before the increase in drag coefficient at $Re = Re_a = 12.3 \times 10^3$, we can observe the rolling up of the vortex from the non-convex part of the model with 0˚ and 30˚ views. After the increasing phase of the drag coefficient at $Re = Re_b = 13.2 \times 10^3$, the vortex collapses from the comparison with $Re = Re_a$. A few small peaks can be observed at $Re = 9.0 \times 10^3$, 11.3×10^3, 12.7×10^3, 15.0×10^3, and 16.2×10^3. These relate to the vortex formation and collapse behind the model because of visualization. This implies that the vortex formation and detachment from behind the model occurred continuously during free fall. **Figure 7** shows the visualization using model$_{45°}$ to help understand vortex detachment.

The figure shows the visualization results and the plot from **Figure 6**. In **Figure 8(d)**, we can observe three small positive peaks at $Re = 9.6 \times 10^3$, 12.1×10^3, and 14.5×10^3. The visualization results shown in **Figure 8(a)**, **Figure 8(b)** focus on after the peaks at $Re = Re_c = 12.6 \times 10^3$. The result of the peak at Re_c shows the vortex growth from the convex portion of the plate as shown in the result using model$_{15°}$ in **Figure 7**. The vortex at this time starts to collapse. At the end of the decreasing phase of $Re = Re_d = 14.3 \times 10^3$ as shown in **Figure 8(c)**, the vortex was shredded from the model plate at Re_d. In addition, the vortex was forming near the plate for the next small peak at $Re = 14.5 \times 10^3$. These results in **Figure 7** and **Figure 8** show that the periodical change in drag coefficient at terminal velocity shown in **Figure 6** was caused by the continuous formation and detachment of vortices.
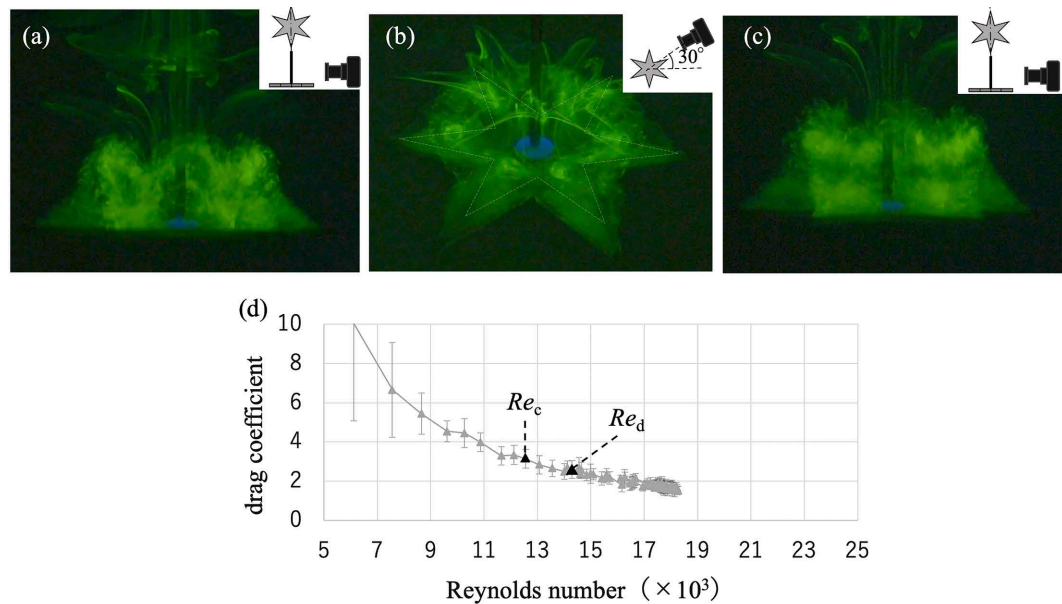
Figure 8. Flow visualization using model$_{45°}$ during the accelerating phase. (a) 0° view of the flow structure at $Re = Re_c$. (b) 30° view of the flow structure at $Re = Re_c$. (c) 0° view of the flow structure at $Re = Re_d$.
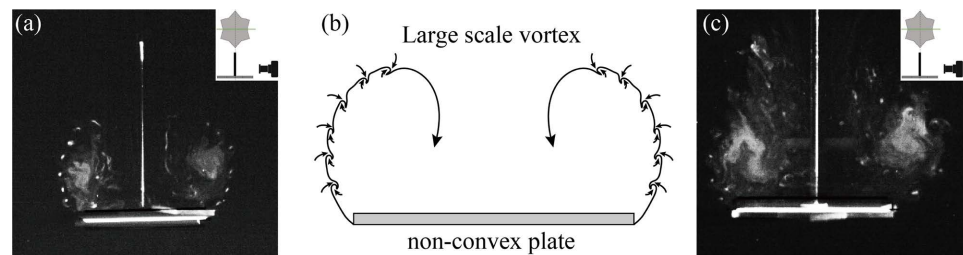

Figure 9. Flow visualization around model$_{15°}$ at the terminal velocity. (a) Vortex formation and flow separation at the decreasing phase of C_d at terminal velocity. (b) Sketch of the flow structure around the plate at $Re = 20 \times 10^3$. (c) Vortex formation and flow separation at terminal velocity during the increasing phase of C_d at terminal velocity.

Figure 9 shows the result of the flow visualization using model$_{15°}$ during terminal velocity. **Figure 9(a)** shows the result at $Re = 19 \times 10^3$. The change in the Reynolds number causes periodic changes in the terminal velocity, as shown in **Figure 6**, such that the model's motion quickly switched between acceleration and deceleration phases. Because the Reynolds number was increasing at this time (**Figure 6**), the result in $Re = 19 \times 10^3$ corresponded to the acceleration phase on terminal velocity. From the visualization, we can observe the large-scale vortices behind the model. In the shear layer, smaller size vortices were formed. **Figure 9(b)** shows the illustration of these vortices. The large-scale vortices were formed with the free fall of the model. The small vortices were formed because of the instabilities in the shear layer. This is known as the Kelvin–Helmholtz instability. We can confirm Kelvin-Helmholtz instability in the wake even in the sphere at $Re = 5000$ [14]. We can confirm this visualization as the vortex was formed from the edge of the plate. The vortices formed in the shear layer with an accelerating plate [15]. **Figure 9(c)** shows the result in the deceleration phase

with the terminal velocity at $Re = 20 \times 10^3$. The wake region shows the breakdown of the vortex. This affects the deceleration of the motion of the model. We can confirm the formation and flow separation of vortices from the edge of the model. The drag coefficient converges from the series of model motions between the release of the model and the terminal velocity while vortices continuously form and detach.

4. Conclusion

We estimated the drag coefficient during the free fall of a non-convex hexagonal thin plate. We developed the non-convex model by cutting off isosceles triangles from a convex hexagonal thin plate. The base angle of the triangle was between θ = 0° to 45°. The drag coefficient of terminal velocity increased with the increase in base angle except for when θ was less than 30°. The drag coefficient during the acceleration phase until terminal velocity decreased with the increase in Reynolds number. We observed the small positive peaks of the drag coefficient owing to the formation and detachment of the vortex at the wake region. In the terminal velocity, the drag coefficient changed periodically due to the vortex formation behind the model. Two types of vortices formed. One was the wake of the model. The vortex grew from the convex part of a plate. The other was related to the instabilities of the shear layer.

Conflicts of Interest

The authors declare no conflicts of interest regarding the publication of this paper.

References

[1]   Fish, F.E. (1996) Transitions from Drag-Based to Lift-Based Propulsion in Mammalian Swimming. *American Zoologist,* **36**, 628-641.
https://doi.org/10.1093/icb/36.6.628

[2]   Wolfgang, M.J., Anderson, J.M., Grosenbaugh, M.A., Yue, D.K. and Triantafyllou, M.S. (1999) Near-Body Flow Dynamics in Swimming Fish. *Journal of Experimental Biology,* **202**, 2303-2327.https://doi.org/10.1242/jeb.202.17.2303

[3]   Borazjani, I. and Daghooghi, M. (2012) The Fish Tail Motion Forms an Attached Leading Edge Vortex. *Proceedings of the Royal Society B: Biological Sciences*, **280**, Article No. 20122071.https://doi.org/10.1098/rspb.2012.2071

[4]   Johansson, L.C. and Norberg, R.A. (2003) Delta-Wing Function of Webbed Feet Gives Hydrodynamic Lift for Swimming Propulsion in Birds. *Nature*, **424**, 65-68.
https://doi.org/10.1038/nature01695

[5]   Kikuchi, K., Uehara, Y., Kubota, Y. and Mochizuki, O. (2014) Morphological Considerations of Fish Fin Shape on Thrust Generation. *Journal of Applied Fluid Mechanics*, **7**, 625-632.https://doi.org/10.36884/jafm.7.04.21358

[6]   Nedić. J., Ganapathisubramani, B. and Vassilicos, J.C. (2013) Drag and Near Wake Characteristics of Flat Plates Normal to the Flow with Fractal Edge Geometries. *Fluid Dynamics Research*, **45**, Article No. 061406.
http://doi.org/10.1088/0169-5983/45/6/061406 061406

[7]   Xiang, Y., Qin, S., Huang, W., Wang, F. and Liu, H. (2018) Trajectory Modes and Wake Patterns of Freely Falling Plates. *Journal of Visualization*, **21**, 433-441. https://doi.org/10.1007/s12650-017-0469-8

[8]   Lau, E.M., Zhang, J.D., Jia, Y.X., Huang, W.X. and Xu C.X. (2019) Vortical Structures in the Wake of Falling Plates. *Journal of Visualization*, **22**, 15-24. https://doi.org/10.1007/s12650-018-0520-4

[9]   He, C. and Liu, Y. (2017) Proper Orthogonal Decomposition of Time-Resolved LIF Visualization: Scalar Mixing in a Round Jet. *Journal of Visualization*, **20**, 789-815. https://doi.org/10.1007/s12650-017-0425-7

[10] Fu, H., He, C. and Liu, Y. (2021) Flow Structures of a Precessing Jet in an Axisymmetric Chamber. *Journal of Visualization*, **24**, 501-515. https://doi.org/10.1007/s12650-020-00722-2

[11] Burgan, H.I. and Aksoy, H. (2022) Daily Flow Duration Curve Model for Ungauged Intermittent Subbasins of Gauged Rivers. *Journal of Hydrology*, **604**, Article No. 127249. https://doi.org/10.1016/j.jhydrol.2021.127249

[12] Breidenthal, R.E. (2008) The Effect of Acceleration on Turbulent Entrainment. *Phys Scr*, **T132**, Article No. 014001. https://doi.org/10.1088/0031-8949/2008/t132/014001

[13] Kikuchi, K., Konno. T., Ichikawa, S., Kubota, Y. and Mochizuki, O. (2013) Unsteady Drag Coefficient of a Falling Sphere in Water. *Transactions of the Japan Society of Mechanical Engineers Series*, **79**, 151-163. (in Japanese) https://doi.org/10.1299/kikaib.79.151

[14] Muammer, O., Engin, P., Besir, S., Huseyin, A., Ozgoren, M., Pinar, E., Sahin, B. and Akilli, H. (2011) Comparison of Flow Structures in the Downstream Region of a Cylinder and Sphere. *International Journal of Heat and Fluid Flow*, **32**, 1138-1146. https://doi.org/10.1016/j.ijheatfluidflow.2011.08.003

[15] Lian, Q.X. and Huang, Z. (1989) Starting Flow and Structures of the Starting Vortex behind Bluff Bodies with Sharp Edges. *Experiments in Fluids*, **8**, 95-103. https://doi.org/10.1007/BF00203070